

Quantitative analysis of seismic velocity tomography in rock burst hazard assessment

Wu Cai · Linming Dou · Siyuan Gong · Zhenlei Li · Shasha Yuan

Received: 15 April 2014 / Accepted: 14 September 2014 / Published online: 23 September 2014
© Springer Science+Business Media Dordrecht 2014

Abstract In order to quantitatively evaluate the relationship between the tomographic images of P wave velocity and rock burst hazard, the seismic velocity tomography was used to generate the P wave velocity tomograms during the retreat of a longwall panel in a coal mine. Subsequently, a novel index (bursting strain energy) was proposed to characterize the mining seismic hazard map. Finally, the structural similarity (SSIM) index in the discipline of image quality assessment was introduced to quantitatively assess the relation between the bursting strain energy index images and the tomographic images of P wave velocity. The results show that the bursting strain energy index is appropriate for quantitative analysis and seems to be better for expressing the mining seismic hazard than the conventional map. The SSIM values of the future bursting strain energy compared with the P wave velocity and the current bursting strain energy reach up to 0.8908 and 0.8462, respectively, which illustrate that the P wave velocity and the bursting strain energy both are able to detect the rock burst hazard region. Specifically, seismic velocity tomography is superior to the bursting strain energy index in the detection range and the precision and accuracy of detection results.

W. Cai · L. Dou (✉) · S. Gong (✉) · Z. Li
State Key Laboratory of Coal Resources and Safe Mining, China University of Mining and
Technology, Xuzhou 221116, China
e-mail: lmdou@cumt.edu.cn

S. Gong
e-mail: gsy_cumt@163.com

W. Cai
e-mail: aaacaiwu@126.com

W. Cai · L. Dou · Z. Li
School of Mines, China University of Mining
and Technology, Xuzhou 221116, China

S. Yuan
Internet of Things (Perception Mine) Research Center, China University of Mining and Technology,
Xuzhou 221008, China

Keywords Rock burst hazard · Seismic hazard · Seismic velocity tomography · Bursting strain energy · Structural similarity (SSIM)

1 Introduction

As the depth and intensity of coal mining increase, mining tremors have been increasing sharply and substantially, and thus, rock burst has become a common security issue in underground coal mines. Rock burst is usually referred to as dynamic catastrophe, which results in casualties and roadway destruction caused by elastic strain energy emitting in a sudden, rapid and violent way from coal or rock mass, often accompanied by an airblast or windblast and violent failures which can disrupt mine ventilation, pose a danger to miners due to flying material, and may also cause a large release of strata gas and propagate explosive dust into the air (Bräuner 1994; Dou et al. 2012a; Jiang et al. 2014).

Kornowski and Kurzeja (2012) stated that any rock burst is connected with or results from a mining tremor but not all the tremors cause rock bursts, and thereby proposed that two kinds of hazards (i.e. seismic hazard and rock burst hazard) should be defined since which one tremor will bring the rock burst cannot be predicted. The tremors, herein corresponding to the rupture events, are observed at scales ranging from laboratory samples to the Earth's crust, including rock failures in laboratory tests and field experiments, landslides, mining-induced seismicity, and crustal earthquakes (Amitrano 2012). Filimonov et al. (2005), Hardy (2003) have verified that rocks under stress emit acoustic waves in the laboratory and microseismic events in mines, namely, acoustic emissions of rocks observed in the laboratory can be considered as a small-scale model of the seismicity of the Earth's crust (Scholz 1968).

Recently, seismic velocity tomography, widely used for inference of stress distribution, has been applied in underground mines for rock burst hazard assessment. As a small-scale technology used in the laboratory, the ultrasonic technology was adopted to study the relationship between the ultrasonic wave velocity and the variation of stress when load is applied to rock masses (Eberhart-Phillips et al. 1989; Meglis et al. 2005; Mitra and Westman 2009; Nur and Simmons 1969; Westman 2004). Especially, the current research found that a power function existed between the P wave velocity and stress (Gong et al. 2012a, b). As a mine-scale, seismic velocity tomography has been widely applied in underground mines. Friedel et al. (1995, 1997) conducted 3-D seismic velocity tomography with existing rock bolts used to mount geophones and as strike points for introducing seismic energy using a sledge hammer at the Homestake gold mine and Lucky Friday silver mine. The results demonstrate that temporal and spatial changes in the local stress field occurred in response to ground failure and stope advancement, respectively. Dou et al. (2012a), He et al. (2011) and Wang et al. (2012) performed 2-D seismic velocity tomography with geophones screwed into rock bolts located along the maingate and controlled explosions along the tailgate. The results manifest that the consistency between locations of strong mining tremors or stress concentration and high-velocity zones exceeded 80 %. Luo et al. (2009) introduced the seismic signals generated by the continuous coal shearer and geophone arrays deployed ahead of the working face to map out the velocity variations as far as 300 m from the face using the tomographic technique. The results indicate that high seismic velocity was related to a high-stress zone while the low seismic velocity was likely a representation of a low stress concentration zone. Luxbacher et al. (2008), Luxbacher (2008) and Hosseini et al. (2012a, b, 2013) adopted mining-induced microseismic events and surface-mounted geophones to generate velocity tomograms. The results indicate that high-velocity regions agreed well with high abutment stresses predicted by numerical modeling and they were observed to

redistribute as longwall face advanced. Integrating with the tomography technology and microseismic monitoring system, Dou et al. (2014), Bańka and Jaworski (2010) and Lurka (2008) conducted near real time tomographic imaging of rock burst hazard during the mining process of the longwall panel. The results show that rock bursts or strong seismic events mainly occurred in zones with high-velocity and/or high-velocity gradient.

As mentioned above, although some quantitative relationships between the wave velocity and stress are obtained in the laboratory, they still do not meet the application requirements due to the complex in situ conditions. In this context, the vast majority of applications are conducted using the P wave velocity distribution for inference of stress field to indirectly detect the regions of rock burst hazard, or directly comparing the velocity distribution map with the locations of seismic events. Therefore, the current analysis and conclusions in the application remain in the subjective and qualitative levels. Nonetheless, it should be certain that the seismic velocity tomography is still an appropriate technology for assessing rock burst hazard. However, how to directly describe the quantitative degree of the seismic velocity tomography in rock burst hazard assessment remains to be further studied.

In this paper, the bursting strain energy index was proposed to characterize the mining seismic hazard map. Subsequently, the structural similarity (SSIM) index in the discipline of image quality assessment was introduced to quantitatively evaluate the correspondence between the bursting strain energy index maps and the tomographic images of P wave velocity. This study may provide a new approach for further research on the quantitative and direct relationship between the seismic velocity and rock burst hazard.

2 Methods

2.1 Seismic velocity tomography

Using the artificially created or mining-induced sources and geophones mounted on the surface or underground, the seismic velocity $V(x, y, z)$ distribution can be inversed in the spatial coverage area of the source–geophone geometry, which depends on the relationship that the velocity along a seismic ray is the raypath distance L divided by the time T to travel between the source and geophone. Suppose that the raypath of the i th seismic wave is L_i with the travel time of T_i , the relationship can be denoted as (Luxbacher et al. 2008):

$$V = \frac{L}{T} \rightarrow VT = L \tag{1}$$

$$T_i = \int_{L_i} \frac{dL}{V(x, y, z)} = \int_{L_i} S(x, y, z)dL \tag{2}$$

$$T_i = \sum_{j=1}^M d_{ij}S_j \quad (i = 1, \dots, N) \tag{3}$$

where $S(x, y, z) = 1/V(x, y, z)$ is the slowness, s/m; d_{ij} is the distance of the i th seismic wave ray crossing the j th grid; N is the total number of rays; and M is the number of voxels. Equation (3) can also be expressed in a matrix form as:

$$T = DS \rightarrow S = D^{-1}T \tag{4}$$

where T is the column vector of travel times ($N \times 1$); S is the column vector of slowness values ($M \times 1$); and D is the matrix of ray distances ($N \times M$).

Usually, the inverse problem of Eq. (4) is either underdetermined or overdetermined. The most effective way to solve this problem is the iterative process. The most referenced iterative methods are algebraic reconstructive technique (ART) and simultaneous iterative reconstructive technique (SIRT) (Gilbert 1972). SIRT is an appropriate algorithm because the solution tends to be converging and diverging slowly, so that the solution is relatively stable (Hosseini et al. 2012b; Luxbacher et al. 2008).

2.2 Bursting strain energy index

The conventional seismic hazard maps were illustrated by seismic events using different circles with radii proportional to epicentral intensities (Kracke and Heinrich 2004). Such images are direct-viewing and vivid, which is convenient for subjective and qualitative analysis, and thereby widely used. It is however not appropriate for quantitative analysis and comparison. Therefore, it is significant to establish a new index that can reflect the seismicity activities and meet the requirements of quantitative analysis.

Benioff (1951) has shown that the elastic strain rebound increment generating an earthquake is proportional to the square root of the energy of the earthquake. Kracke and Heinrich (2004) indicated that the stress release of earthquake seems to be more appropriate to characterize earthquake sources than the energy release. Thus, it is advantageous to choose the square root of the released energy of earthquakes as expressing the seismic hazard. As a consequence, a new index (bursting strain energy) can be defined as:

$$E_{ej} = \log_{10} \left(\frac{\sum \sqrt{E_i}}{A \cdot P} \right) \quad (5)$$

where E_{ej} is the bursting strain energy of the j th statistical region, $\log_{10} \sqrt{J}$; E_i is the energy of the i th seismic event which belongs to the j th statistical region, J ; A is the area of the j th statistical region, m^2 ; P is the statistical time, day.

2.3 Structural similarity index

After the tomographic images of the P wave velocity and the mining seismic hazard maps were obtained using the seismic velocity tomography and the bursting strain energy index, respectively, the consistency between them was usually distinguished subjectively by the human visual system in the past. However, this assessment result often varies with different individuals, and there is no criterion for reference, just remaining in the levels of qualitative analysis.

Structural similarity theory shows that natural image signals are highly structured: Their pixels exhibit strong dependencies, especially when they are spatially proximate, and these dependencies carry important information about the structure of objects in the visual scene. Based on the assumption that the human visual system is highly adapted to extract structure information from the viewing field, a novel index called SSIM (Wang et al. 2004) was proposed:

$$\text{SSIM}(X, Y) = \frac{(2\mu_x\mu_y + C_1)(2\sigma_{xy} + C_2)}{(\mu_x^2 + \mu_y^2 + C_1)(\sigma_x^2 + \sigma_y^2 + C_2)} \quad (6)$$

where μ_x , μ_y are the mean values of image signals X and Y , respectively, estimated as the signal luminance; σ_x , σ_y are the standard deviations, estimated as the signal contrast; σ_{xy} is

the covariance, estimated as the signal structure; $C_1 = (K_1L)^2$ and $C_2 = (K_2L)^2$, L is the dynamic range of the pixel values, and $K_1 = 0.01$ and $K_2 = 0.03$ by default (Wang et al. 2004).

The maximum value of SSIM index is 1, which is only reachable in the case of two identical sets of data. Moreover, the larger the value of SSIM index, the higher the consistency of the two images will be.

3 A case study

3.1 Site description

The Yuejin coal mine, owned and operated by Yima Coal Group Company, is located in the west of Henan province, China. Currently, mining activity at the Yuejin coal mine occurs to LW 25110, as shown in Fig. 1. The panel is fairly deep with about 970 m of overburden. The longwall fully mechanized top coal caving method is used to retreat the panel. LW 25110 is adjacent to the gob in the north with F16 thrust fault in the south and solid coal seam in the east and west. The length and the width of the panel are approximately 865 and 191 m, respectively. The coal seam thickness ranges from 8.4 to 13.2 m (about 11.5 m in average) with an average dip angle 12°. The seam is overlain successively by 18 m of mudstone, 1.5 m of coal, 4 m of mudstone, and 190 m of glutenite, and successively underlain by 4 m of mudstone and 26 m of sandstone.

Microseismic monitoring in mines allows for calculation of microseismic event source location, energy or magnitude, and source mechanisms, which can be further used as tomography to infer the state of stress and assess rock burst hazard. Since April 22, 2011, the microseismic monitoring system called “ARAMIS M/E” that was developed by the institute of innovative technologies EMAG of Poland has been installed in the Yuejin coal mine. Figure 1 displays the panel geometry and relative receiver locations, which includes six permanent stations (blue triangles) assembled on the decline and main entries and ten

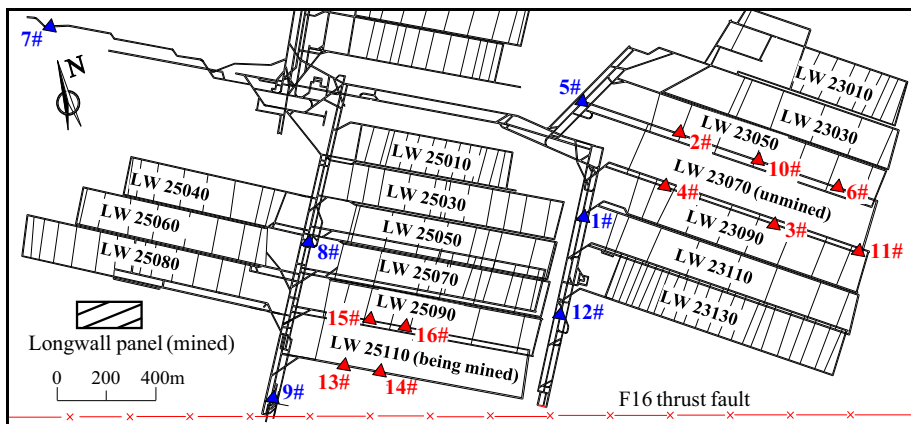


Fig. 1 Layout of the microseismic monitoring system installed in the Yima Yuejin coal mine, Henan Province, China. Red triangles are temporary stations which can be moved parallel to the coal face advances and blue triangles are permanent stations

temporary stations (red triangles) mounted on the tailgate and maingate entries that can be moved parallel to coal face advances.

3.2 P wave velocity inversion

The seismic velocity tomography was conducted with the microseismic monitoring system and mining-induced seismic events. Through picking the P wave arrival time after the seismic wave passes through the rock mass, the data were analyzed using MINESOS-TOMO program (Gong 2010) to generate velocity tomograms with SIRT. In order to improve the inversion efficiency, the seismic velocity tomography on LW 25110 was performed using the selected stations (8#, 9#, 12#, 13#, 14#, 15#, and 16#) and the seismic events located in the target areas. Moreover, the events recorded by more than five stations were adopted to avoid creating artificial anomaly in tomograms. In the process of seismic velocity tomography, the constant velocity equal to 4 km/s was assumed in the research area to calculate the location of seismic events and perturb the first iteration. The voxel size of about $30\text{ m} \times 30\text{ m} \times 100\text{ m}$ was considered due to the fact that the seismic station geometry in underground coal mining longwall panels did not vary significantly in vertical direction and thereby did not constrain the events well vertically. To reduce the indeterminacy, a maximum velocity constraint of 6.0 km/s was imposed. Ultimately, the three-dimensional images of P wave velocity were created and sliced at approximately coal seam level (see Fig. 2). Symbols in the figure show positions of the future seismic events.

3.3 Bursting strain energy generation

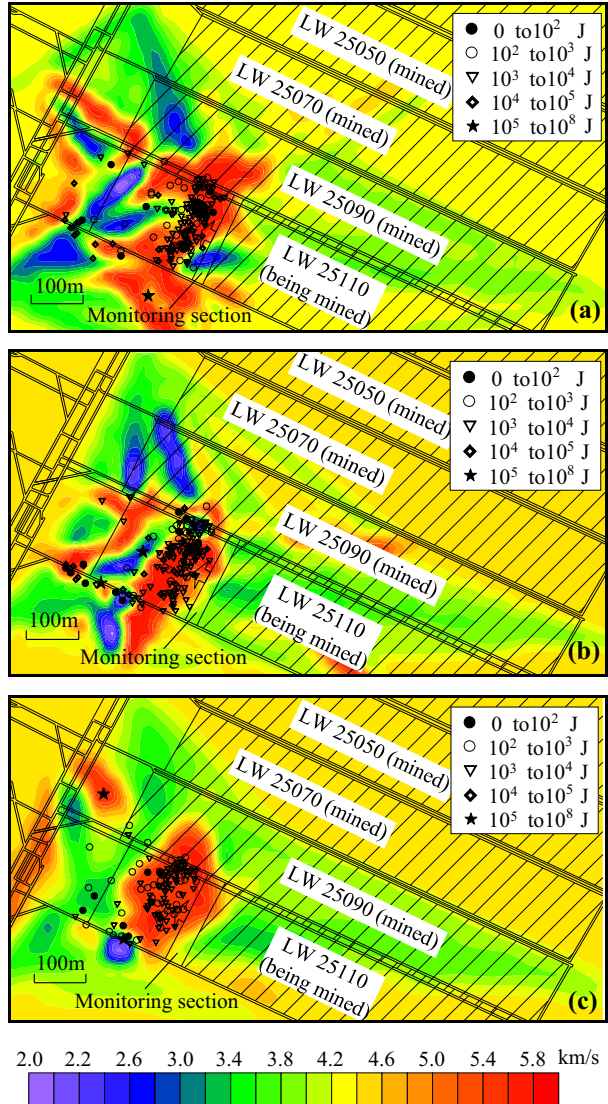
According to the concept of spatially smoothed seismicity as the earthquake hazard calculation introduced by Frankel (1995) and Frankel et al. (2000), the seismic events were considered as point sources. In the process of the statistical calculation, the main parameter (statistical smoothed radius R) was determined by the hypocenter location error calculated by the numerical emulation method (Gong et al. 2010). In order to avoid omitting individual seismic events which may cause the results to lack fidelity, the relation between the grid spacing S and the statistical smoothed radius r should be satisfied as: $S \leq \sqrt{2}R$. Figure 3 displays the sketch map of the spatially statistical smoothed model, whose specific processes of the calculation are the following: each grid node corresponds to a statistical round region; seismic events belonging to each statistical round region are selected to calculate the bursting strain energy value as a function of Eq. (5), which is then considered as the value of its corresponding grid node; finally, the bursting strain energy map, based on the values of all grid nodes, can be generated using the interpolation.

The methods mentioned above allow us to ascertain the parameters: $R = 30\text{ m}$, $S = 10\text{ m}$. Consequently, maps of bursting strain energy index during different periods were obtained (see Fig. 4). Symbols in the figure show positions of the seismic events adopted to generate the map of bursting strain energy.

3.4 Structural similarity assessment

As seen from Figs. 2 and 4, the detection zones using the seismic velocity tomography are larger than the hazard areas described by the bursting strain energy index. In order to ensure the assessment accuracy of SSIM index between the velocity tomographic images and the bursting strain energy maps, the tomographic images need to be cut into the same

Fig. 2 Plan view of seismic velocity tomograms at coal seam on LW 25110. Symbols show positions of the future seismic events. The monitoring section indicates total area mined over the inversion period. (a) Plan view of velocity tomogram at coal seam obtained from seismic events between April 1, 2012 and April 20, 2012. Symbols show positions of seismic events that occurred between April 21, 2012 and May 21, 2012. (b) Plan view of velocity tomogram at coal seam obtained from seismic events between April 16, 2012 and May 8, 2012. Symbols show positions of seismic events that occurred between May 9, 2012 and June 9, 2012. (c) Plan view of velocity tomogram at coal seam obtained from seismic events between May 8, 2012 and June 7, 2012. Symbols show positions of seismic events that occurred between June 8, 2012 and July 8, 2012

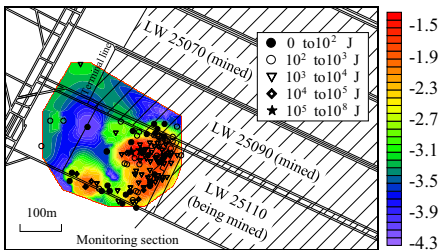
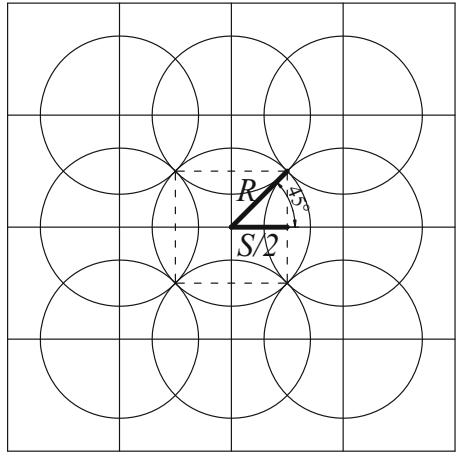


size and shape of the bursting strain energy maps, as shown in Fig. 5. All the images are meanwhile filled with the same color scale. As a result, the SSIM index values were calculated between the tomographic images and the current and the future bursting strain energy maps, as shown in Table 1.

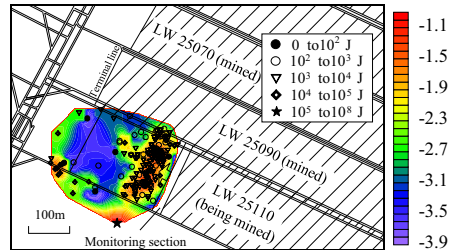
4 Results and discussion

Figure 2 reveals evidence of high-velocity zones ahead of the face corresponding to areas where front abutment stresses would be expected. Additionally, a low-velocity zone can be

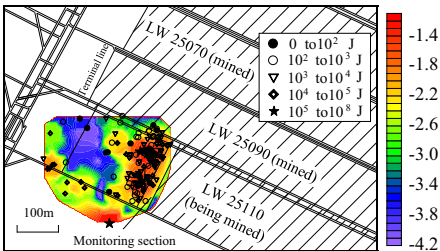
Fig. 3 Sketch map of the spatially smoothed model. S is the grid spacing and R is the statistical smoothed radius



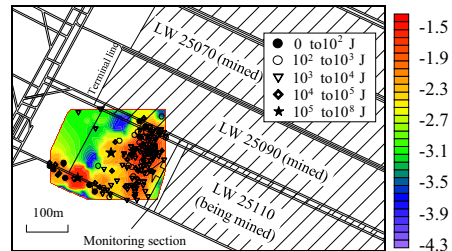
(a1) April 1 to April 20, 2012



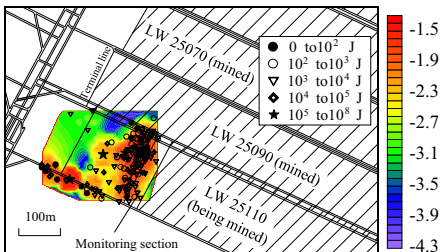
(b1) April 21 to May 21, 2012



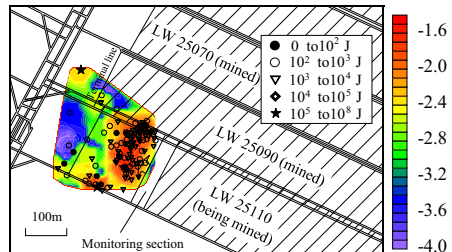
(a2) April 16 to May 8, 2012



(b2) May 9 to June 9, 2012



(a3) May 8 to June 7, 2012



(b3) June 8 to July 8, 2012

Fig. 4 Maps of the bursting strain energy index (Unit: $\log_{10} \sqrt{J}$). Symbols show positions of the seismic events adopted to generate the map of bursting strain energy. (a) Current distribution of the bursting strain energy. (b) Future distribution of the bursting strain energy

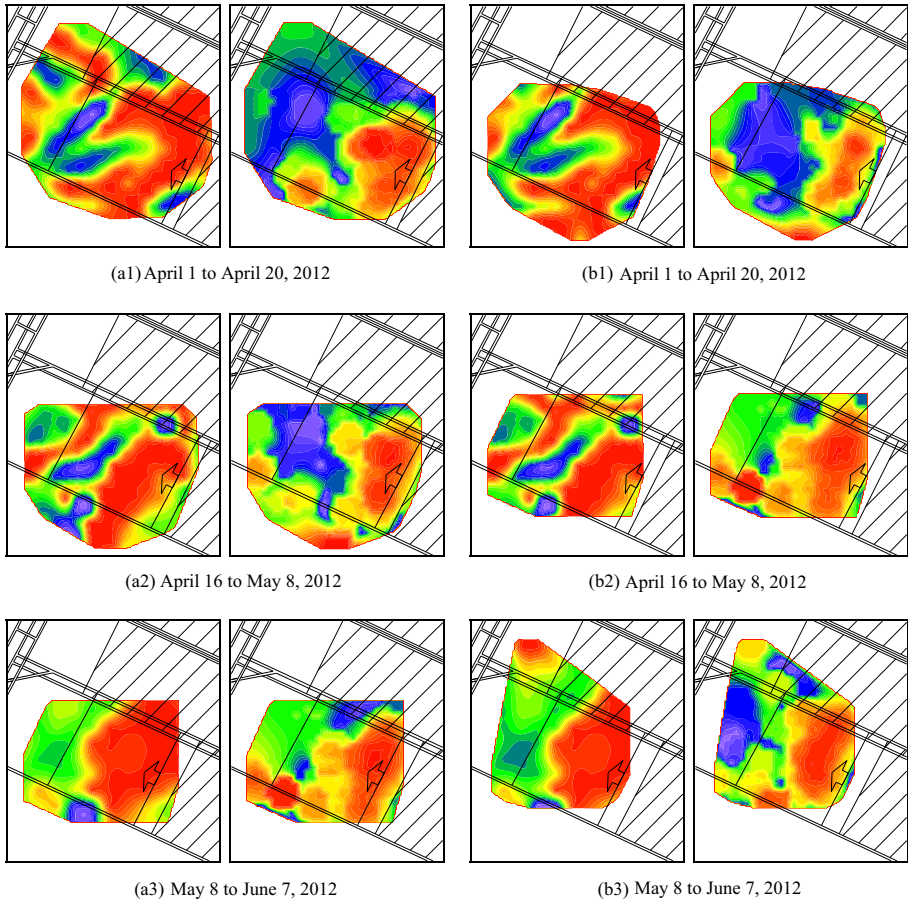


Fig. 5 Comparison diagrams between the P wave velocity and the bursting strain energy. (a) Velocity images in the left and the current bursting strain energy maps in the right. (b) Velocity images in the left and the future bursting strain energy maps in the right

seen behind the face corresponding to the location of the gob. These features consistently redistribute with face advance, and a low-velocity zone in the gob area is also consistently present. Besides, almost all of the seismic events occur in zones with high-velocity and/or high-velocity gradient. This is in good agreement with previous results presented by Bańka and Jaworski (2010), Dou et al. (2014), and Lurka (2008). Especially in the high-velocity zone near the terminal line of LW 25090 (see Fig. 2c), there occurred a unique strong seismic event with an intensity $\geq 10^5$ J.

Figure 4 displays the similar feature of high bursting strain energy ahead of the face, which consistently redistributes with face advance. Moreover, the bursting strain energy maps not only contain the information of conventional seismic hazard maps characterized by different symbols (see Fig. 4), but also provide more information and more obvious hazard areas. These results allow us to recognize that the bursting strain energy map is appropriate for quantitative analysis and seems to be better for expressing mining seismic hazard than the conventional map.

Table 1 Structural similarity index (SSIM) values

SSIM values	Comparison parameters between		
	P wave velocity and current bursting strain energy	P wave velocity and future bursting strain energy	Current and future bursting strain energy
Current time period			
April 1 to April 20, 2012	0.7932	0.8417	0.7814
April 16 to May 8, 2012	0.8584	0.8908	0.8424
May 8 to June 7, 2012	0.9048	0.8876	0.8462

Both the tomographic images of the P wave velocity and the bursting strain energy maps in this study were generated by seismic events. Since the seismic events are part of the mining operations and do not need a person to physically initiate them, there is no disruption to production, and thereby they have the potential to provide an opportunity for remote and long-term monitoring at regular time intervals. Therefore, these two technologies are promising to continuously monitor the rock burst hazard in a mine (especially in the panel being mined, as shown in Figs. 2 and 4) so that precautionary measures can be taken, improving safety for miners working underground and positively impacting productivity.

Table 1 shows the SSIM index values between the tomographic images of the P wave velocity and the current and the future bursting strain energy maps, which can allow us to conclude:

1. The SSIM index values between the P wave velocity images and the future bursting strain energy maps exceed 0.8417, which illustrates that the consistency between them exceeds 84.17 %. It is verified that seismic velocity tomography is a powerful tool to evaluate rock burst hazard from the perspective of quantitative assessment.
2. The maximum value of SSIM index between the P wave velocity images and the current bursting strain energy maps reaches 0.9048, which manifests that the vast majority information of the P wave velocity image can be characterized by the bursting strain energy map, indicating that the bursting strain energy index may be used to assess rock burst hazard.
3. The SSIM index values between the current and the future bursting strain energy maps are between 0.7814 and 0.8462, which once again demonstrates the feasibility of rock burst hazard assessment through the bursting strain energy index. Moreover, the conclusion that the density nephogram of microseismic events (Dou et al. 2012b; Tang and Xia 2010) and the contour map of apparent stress (Tang et al. 2011) could be employed to predict rock burst seems to be verified.
4. The SSIM index values between the P wave velocity images and the future bursting strain energy maps are both larger than that of between the current and the future bursting strain energy maps, which allows us to recognize that seismic velocity tomography is superior to the bursting strain energy index for rock burst hazard assessment in the precision and accuracy of detection results.

The seismic velocity tomography was conducted with the microseismic monitoring system and mining-induced seismic events, which allows for monitoring over large areas of the source–geophone geometry, such as an entire mine, or active panel in a mine. The bursting strain energy index, however, only monitors over the areas where the seismic

events take place. Usually, areas where the seismic events occur are much smaller than that of the source–geophone geometry. In this context, the seismic velocity tomography appears to be the superior technique for rock burst hazard assessment in the detection range.

Finally, it is important to note that the interpretation should be carefully made for the area with low or inadequate seismic events density, especially in the seismic velocity tomography which would not be appropriate with relatively few mining-induced micro-seismic events unless a dense receiver array is implemented.

5 Conclusions

1. Compared with the conventional seismic hazard map, the bursting strain energy map is appropriate for quantitative analysis and seems to be better for expressing the mining seismic hazard.
2. The SSIM values of the future bursting strain energy compared with the P wave velocity and the current bursting strain energy reach up to 0.8908 and 0.8462, respectively, which illustrate that the P wave velocity and the bursting strain energy both are able to detect the rock burst hazard region with high efficiency.
3. Seismic velocity tomography is superior to the bursting strain energy index for rock burst hazard assessment in the detection range, and the precision and accuracy of detection results.
4. In the future, more traditional methods should be seized to conduct together with the seismic velocity tomography, as this could lead the ability to quantify the results of tomograms. With these recommendations explored, the seismic velocity tomography in underground coal mines can be improved, contributing to a safer and more productive environment.

Acknowledgments The Institute of Rock Pressure (Henan Dayou Energy Limited Company) and the Yuejin coal mine provided the microseismic data. In particular, we would like to extend a special thanks to Dr. Li Xuwei, Dr. Qiao qiuqiu, and two reviewers for their useful comments and constructive suggestions, which greatly improved the quality of this manuscript. We gratefully acknowledge the financial support for this work provided by the National Natural Science Foundation of China (51174285, 51204165), the National Basic Research Program of China (2010CB226805), the Jiangsu Natural Science Foundation (BK20130183), and the Projects supported by the Priority Academic Program Development of Jiangsu Higher Education Institution (SZBF2011-6-B35).

References

- Amitrano D (2012) Variability in the power-law distributions of rupture events. *Eur Phys J Spec Top* 205:199–215. doi:10.1140/epjst/e2012-01571-9
- Baňka P, Jaworski A (2010) Possibility of more precise analytical prediction of rock mass energy changes with the use of passive seismic tomography readings. *Arch Min Sci* 55:723–731
- Benioff H (1951) Crustal strain characteristics derived from earthquake sequences. *Trans Am Geophys Union* 32:508–514
- Bräuner G (1994) Rockbursts in coal mines and their prevention. AA Balkema, Rotterdam
- Dou L, Chen T, Gong S, He H, Zhang S (2012a) Rockburst hazard determination by using computed tomography technology in deep workface. *Saf Sci* 50:736–740. doi:10.1016/j.ssci.2011.08.043
- Dou L, He J, Gong S, Song Y, Liu H (2012b) A case study of micro-seismic monitoring: goaf water-inrush dynamic hazards. *J China Univ Min Technol* 41:20–25

- Dou L, Cai W, Gong S, Han R, Liu J (2014) Dynamic risk assessment of rock burst based on the technology of seismic computed tomography detection. *J China Coal Soc* 39:238–244. doi:[10.13225/j.cnki.jccs.2013.2016](https://doi.org/10.13225/j.cnki.jccs.2013.2016)
- Eberhart-Phillips D, Han D-H, Zoback MD (1989) Empirical relationships among seismic velocity, effective pressure, porosity, and clay content in sandstone. *Geophysics* 54:82–89. doi:[10.1190/1.1442580](https://doi.org/10.1190/1.1442580)
- Filimonov Y, Lavrov A, Shkuratnik V (2005) Effect of confining stress on acoustic emission in ductile rock. *Strain* 41:33–35. doi:[10.1111/j.1475-1305.2004.00182.x](https://doi.org/10.1111/j.1475-1305.2004.00182.x)
- Frankel A (1995) Mapping seismic hazard in the central and eastern United States. *Seismol Res Lett* 66:8–21. doi:[10.1785/gssrl.66.4.8](https://doi.org/10.1785/gssrl.66.4.8)
- Frankel A et al (2000) USGS national seismic hazard maps. *Earthq Spectra* 16:1–19. doi:[10.1193/1.1586079](https://doi.org/10.1193/1.1586079)
- Friedel M, Jackson M, Scott D, Williams T, Olson M (1995) 3-D tomographic imaging of anomalous conditions in a deep silver mine. *J Appl Geophys* 34:1–21. doi:[10.1016/0926-9851\(95\)00007-0](https://doi.org/10.1016/0926-9851(95)00007-0)
- Friedel M, Scott D, Williams T (1997) Temporal imaging of mine-induced stress change using seismic tomography. *Eng Geol* 46:131–141. doi:[10.1016/S0013-7952\(96\)00107-X](https://doi.org/10.1016/S0013-7952(96)00107-X)
- Gilbert P (1972) Iterative methods for the three-dimensional reconstruction of an object from projections. *J Theor Biol* 36:105–117. doi:[10.1016/0022-5193\(72\)90180-4](https://doi.org/10.1016/0022-5193(72)90180-4)
- Gong S (2010) Research and application of using mine tremor velocity tomography to forecast rockburst danger in coal mine. China University of Mining and Technology, Xuzhou, China
- Gong S, Dou L, Cao A, He H, Du T, Jiang H (2010) Study on optimal configuration of seismological observation network for coal mine. *Chinese J Geophys-CH* 53:457–465. doi:[10.3969/j.issn.0001-5733.2010.02.025](https://doi.org/10.3969/j.issn.0001-5733.2010.02.025)
- Gong S, Dou L, He J, He H, Lu C, Mu Z (2012a) Study of correlation between stress and longitudinal wave velocity for deep burst tendency coal and rock samples in uniaxial cyclic loading and unloading experiment. *Rock and Soil Mech* 33:41–47
- Gong S, Dou L, Xu X, He J, Lu C, He H (2012b) Experimental study on the correlation between stress and P-wave velocity for burst tendency coal-rock samples. *J Min Saf Eng* 29:67–71
- Hardy Jr HR (2003) Acoustic emission/microseismic activity: volume 1: principles, techniques and geo-technical applications. Taylor & Francis
- He H, Dou L, Li X, Qiao Q, Chen T, Gong S (2011) Active velocity tomography for assessing rock burst hazards in a kilometer deep mine. *Min Sci Technol* 21:673–676. doi:[10.1016/j.mstc.2011.10.003](https://doi.org/10.1016/j.mstc.2011.10.003)
- Hosseini N, Oraee K, Shahriar K, Goshtasbi K (2012a) Passive seismic velocity tomography and geostatistical simulation on longwall mining panel. *Arch Min Sci* 57:139–155. doi:[10.2478/v10267-012-0010-9](https://doi.org/10.2478/v10267-012-0010-9)
- Hosseini N, Oraee K, Shahriar K, Goshtasbi K (2012b) Passive seismic velocity tomography on longwall mining panel based on simultaneous iterative reconstructive technique (SIRT). *J Cent South Univ* 19:2297–2306. doi:[10.1007/s11771-012-1275-z](https://doi.org/10.1007/s11771-012-1275-z)
- Hosseini N, Oraee K, Shahriar K, Goshtasbi K (2013) Studying the stress redistribution around the longwall mining panel using passive seismic velocity tomography and geostatistical estimation. *Arab J Geosci* 6:1407–1416. doi:[10.1007/s12517-011-0443-z](https://doi.org/10.1007/s12517-011-0443-z)
- Jiang Y, Pan Y, Jiang F, Dou L, Ju Y (2014) State of the art review on mechanism and prevention of coal bumps in China. *J China Coal Soc* 39:205–213. doi:[10.13225/j.cnki.jccs.2013.0024](https://doi.org/10.13225/j.cnki.jccs.2013.0024)
- Kornowski J, Kurzeja J (2012) Prediction of rockburst probability given seismic energy and factors defined by the expert method of hazard evaluation (MRG). *Acta Geophys* 60:472–486. doi:[10.2478/s11600-012-0002-3](https://doi.org/10.2478/s11600-012-0002-3)
- Kracke DW, Heinrich R (2004) Local seismic hazard assessment in areas of weak to moderate seismicity—case study from Eastern Germany. *Tectonophysics* 390:45–55. doi:[10.1016/j.tecto.2004.03.023](https://doi.org/10.1016/j.tecto.2004.03.023)
- Luo X, King A, Van de Werken M (2009) Tomographic imaging of rock conditions ahead of mining using the shearer as a seismic source—a feasibility study. *IEEE Trans Geosci Remote Sens* 47:3671–3678. doi:[10.1109/tgrs.2009.2018445](https://doi.org/10.1109/tgrs.2009.2018445)
- Lurka A (2008) Location of high seismic activity zones and seismic hazard assessment in Zabrze Biełzowice coal mine using passive tomography. *J China Univ Min Technol* 18:177–181. doi:[10.1016/S1006-1266\(08\)60038-3](https://doi.org/10.1016/S1006-1266(08)60038-3)
- Luxbacher KD (2008) Time-lapse passive seismic velocity tomography of longwall coal mines: a comparison of methods. Virginia Polytechnic Institute and State University, Blacksburg, Virginia
- Luxbacher K, Westman E, Swanson P, Karfakis M (2008) Three-dimensional time-lapse velocity tomography of an underground longwall panel. *Int J Rock Mech Min Sci* 45:478–485. doi:[10.1016/j.ijrmms.2007.07.015](https://doi.org/10.1016/j.ijrmms.2007.07.015)
- Meglis I, Chow T, Martin C, Young R (2005) Assessing in situ microcrack damage using ultrasonic velocity tomography. *Int J Rock Mech Min Sci* 42:25–34. doi:[10.1016/j.ijrmms.2004.06.002](https://doi.org/10.1016/j.ijrmms.2004.06.002)

- Mitra R, Westman E (2009) Investigation of the stress imaging in rock samples using numerical modeling and laboratory tomography. *Int J Geotech Eng* 3:517–525
- Nur A, Simmons G (1969) Stress-induced velocity anisotropy in rock: an experimental study. *J Geophys Res* 74:6667–6674. doi:[10.1029/JB074i027p06667](https://doi.org/10.1029/JB074i027p06667)
- Scholz C (1968) The frequency-magnitude relation of microfracturing in rock and its relation to earthquakes. *B Seismol Soc Am* 58:399–415
- Tang LZ, Xia KW (2010) Seismological method for prediction of areal rockbursts in deep mine with seismic source mechanism and unstable failure theory. *J Cent South Univ T* 17:947–953. doi:[10.1007/s11771-010-0582-5](https://doi.org/10.1007/s11771-010-0582-5)
- Tang C, Wang J, Zhang J (2011) Preliminary engineering application of microseismic monitoring technique to rockburst prediction in tunneling of Jinping II project. *J Rock Mech and Geotech Eng* 2:193–208
- Wang Z, Bovik AC, Sheikh HR, Simoncelli EP (2004) Image quality assessment: from error visibility to structural similarity. *IEEE T Image Process* 13:600–612. doi:[10.1109/TIP.2003.819861](https://doi.org/10.1109/TIP.2003.819861)
- Wang S, Mao D, Du T, Chen F, Feng M (2012) Rockburst hazard evaluation model based on seismic CT technology. *J China Coal Soc* 37:1–6
- Westman EC (2004) Use of tomography for inference of stress redistribution in rock. *IEEE T Ind Appl* 40(1413–1417):2004. doi:[10.1109/TIA.834133](https://doi.org/10.1109/TIA.834133)